

# Observation of quasi-coherent density fluctuation in scrape-off layer enhancing boundary transport in high- $\beta_N$ hybrid plasmas on DIII-D

R. Hong,<sup>1</sup> T. L. Rhodes,<sup>1</sup> Z.-Y. Li,<sup>2</sup> H. Wang,<sup>3</sup> L. Zeng,<sup>1</sup>

K. Barada,<sup>1</sup> G. Wang,<sup>1</sup> J. G. Watkins,<sup>4</sup> and W. A. Peebles<sup>1</sup>

<sup>1</sup>*Physics and Astronomy Department, University of California, Los Angeles, CA 90095, USA*

<sup>2</sup>*Oak Ridge Associated Universities, Oak Ridge, TN 37831, USA*

<sup>3</sup>*General Atomics, San Diego, CA 92121, USA*

<sup>4</sup>*Sandia National Laboratories, Post Office Box 969, Livermore, CA 94551, USA*

## Abstract

We report the observation of a quasi-coherent density fluctuation (QCF) by the Doppler backscattering system in the scrape-off layer (SOL) region of the DIII-D tokamak. This QCF is observed in high power, high performance hybrid plasmas with near double-null divertor (DND) shape during the electron cyclotron heating period. This mode is correlated with a steepened SOL density profile, and leads to significantly elevated particle and heat fluxes between ELMs. The SOL QCF is a long-wavelength ion-scale fluctuation ( $k_\theta \rho_s \approx 0.2 - 0.4$  and  $k_r \rho_s \approx 0.03$ ), and propagates in the ion diamagnetic direction in the plasma frame. Its radial expanse is about 1.5–2 cm, well beyond the typical width of heat flux  $\lambda_q$  on DIII-D. Also, the SOL QCF does not show any clear dependence on the effective SOL collisionality, and thus may raise issues on the control of plasma-material interactions in low collisionality plasmas in which the blob-induced transport is reduced. A linear simulation using BOUT++ with a 5-field reduced model is performed and compared with experimental observations. In simulation results, an interchange-like density perturbation can be driven by the SOL density gradient, and its peak location and the radial width of the density perturbation are in agreement with the experimental observations.

## I. INTRODUCTION

The edge and scrape-off layer (SOL) turbulence plays an important role in tokamaks, as it can affect the boundary plasma profiles, which in turn set the boundary conditions for the core plasma, and thus determines the overall confinement properties of the discharge [1–4]. The SOL turbulent transport can influence the particle and heat load distributions on the plasma-facing components [5]. These processes have strong impacts on the impurity concentrations and neutral pressures in the peripheral region, which will also affect the confinement and stability of plasmas.

As observed in numerous experiments [6–10], the radial turbulent transport in the SOL region is dominated by blobs, i.e., intermittent filamentary structures [11]. The effects of blobs on the SOL transport have been investigated in L-mode and between ELMs H-mode plasmas [12–15], to validate edge transport modeling of the SOL for future fusion devices, such as ITER. The statistical properties and intermittent features of the SOL turbulence are found to be similar in both *L*-plasmas and moderately powered *H*-plasmas [10]. Also, the blob-induced transport increases as the density or the SOL collisionality is raised [8, 16].

When the tokamak is operated in high-power, high-performance scenarios, it is unclear whether the blobs are still the only dominant turbulent structure in the SOL region, because the boundary plasma profiles behave differently from those with low-to-moderate power injection. For instance, a shelf-like density profile is observed to span the separatrix, and leads to a steepened density gradient in the SOL region of hybrid plasmas with near-double null divertor (DND) configuration during high-power, high-performance operation ( $P_{\text{in}}$  up to 15 MW,  $H_{98} = 1.4\text{--}1.8$  and  $\beta_{\text{N}} = 3\text{--}4$ ) [17, 18]. Such steepened boundary profiles may be able to drive SOL fluctuations, other than the blobs, that are large enough to influence the transport process. The studies on the edge and SOL turbulent transport in these high-power hybrid plasmas are still limited. Thus, the identification of the dominant SOL turbulence structures will improve our understanding, and hence catalyze the optimization, of the high-power, high-performance hybrid scenarios.

For many years, SOL turbulence has been extensively investigated in both toroidal and linear fusion devices by the means of Langmuir probes [6, 8–10]. However, the use of probes in high power operations are limited, as it can be easily melted by the high heat flux and leads to increased impurity contamination. In this study, the SOL turbulence are mainly investigated by the Doppler backscattering (DBS) systems [19]. Based on the DBS measurements, we report the experimental observation of a quasi-coherent density fluctuation (QCF) in the SOL region at

the low-field-side (LFS) midplane during the high-power hybrid operation. This SOL QCF is a long-lived, ion-scale fluctuation between ELMs during the electron cyclotron heating, which is distinct from the intermittent and ‘bursty’ events such as blobs. The SOL QCF is highly correlated with substantially elevated particle and heat fluxes into the divertors, and likely driven by the steepened SOL pressure gradient due to the shelf-like density profile across the separatrix. Also, the SOL QCF does *not* depend on the effective SOL collisionality, and thus may be an issue for the control of plasma-material interactions in low collisionality plasmas in which the blob-induced transport is expected to be reduced.

This paper is organized as follows. Sec. II describes the experimental arrangement and major diagnostics used in this study. In Sec. III we describe the general patterns and characteristics of the SOL QCF measured by DBS systems and examine the influence of boundary profiles on the SOL QCF. Results from a linear simulation using BOUT++ are also shown in this section. In Sec. IV, we briefly compare the experimental observations and the linear simulation results. Some different features of the SOL QCF from the blobs, as well as the implications to the boundary transport and PMI studies, are also discussed. Section V summarizes the major findings and conclusions.

## II. EXPERIMENTAL ARRANGEMENT

In this study, all discharges use the near double-null-divertor (DND) configuration (Fig. 1) [17, 20]. These plasmas are featured by a slight magnetic bias toward the upper (‘primary’) divertor, i.e.,  $dR_{\text{sep}}$  ranges from +0.5 to +0.7 cm, where  $dR_{\text{sep}}$  is the radial separation between the primary and secondary separatrix at the outer midplane. The ion  $\nabla B$  drift direction is away from the primary (upper) divertor.

These high-performance hybrid plasmas are characterized by high energy confinement ( $H_{98} = 1.4\text{--}1.8$ ) and high- $\beta_N$  (3–4). Representative plasma parameters are: plasma current  $I_p = 1.0$  MA, the toroidal field  $B_T = 2.0$  T, the edge safety factor  $q_{95} = 6$ , and total power input  $P_{\text{in}} = 11\text{--}15$  MW. The neutral beam injection (NBI) provides up to 11.5 MW power input. The electron cyclotron heating (ECH) system is configured for on-axis heating and current drive with up to 3.5 MW. Line-averaged density was constrained to no more than  $5.5 \times 10^{19} \text{ m}^{-3}$  (about 60% of the Greenwald limit) during the ECH to avoid cutoff or reflection. Also, argon seeding has been employed in some discharges, but it does *not* seem to change the behavior of the quasi-coherent density

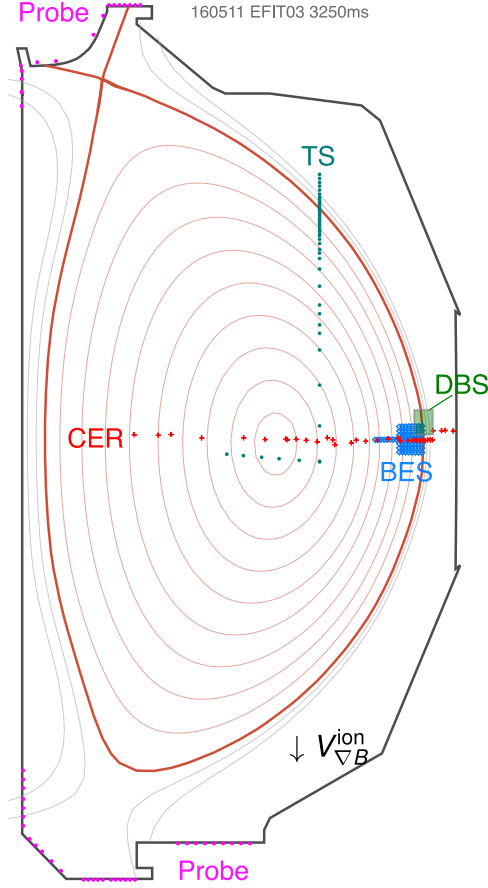


Figure 1. Cross-sectional shape of discharges studied. Positions of major diagnostics are shown: Thomson scattering (teal), BES (blue), CER spectroscopy (red), Langmuir probe (magenta), and DBS (green).

fluctuation in the SOL.

The core and pedestal electron density and temperature in the mainchamber (upstream) are measured by the Thomson scattering system [21] (teal in Fig. 1), while divertor electron density and temperature (downstream) are measured by fixed Langmuir probes (magenta in Fig. 1) [22]. The charge exchange recombination (CER) spectroscopy [23] provides carbon impurity temperature and density, as well as toroidal and poloidal rotation speeds, at points along the outboard midplane (red in Fig. 1). These impurity ion profiles can be used to derive the radial electric field profiles using the carbon ion force balance equation. A 2D array of high sensitivity beam emission spectroscopy (BES) [24] is deployed to measure the low- $k$  (e.g.,  $k_{\theta} < 3 \text{ cm}^{-1}$ ) density fluctuations at the pedestal region (blue in Fig. 1). An 8-channel Doppler backscattering (DBS) system is used to measure turbulent flows and low-to-intermediate- $k$  density fluctuations [19]. The cutoff layer and the wavenumbers of the scattered positions of the millimeter waves at 8 different frequencies

emitted by the DBS system are calculated using the 3D ray-tracing code GENRAY [25]. In this study, DBS measurements cover the region across the separatrix, i.e.,  $0.9 < \psi_n < 1.1$ , where  $\psi_n$  is the normalized poloidal magnetic flux surface function (green in Fig. 1).

### III. RESULTS

#### A. Basic characteristics of SOL QCF

We first explore some basic features of this quasi-coherent density fluctuation, such as mode structures, phase velocities, and some statistical properties. The SOL quasi-coherent fluctuation (QCF) is observed between the ELMs when ECH is applied in addition to the 10 MW neutral beam injection (Fig. 2(a)). The burst of the SOL QCF can be resolved spectrally and temporally by the DBS system (Fig. 2(c)–(e)). The cutoff locations of first three channels are in the SOL region, and other channels locate at the pedestal ( $0.9 < \rho \leq 1.0$ ). The frequency of such density fluctuation spans from  $-1.5$  MHz through  $-2.2$  MHz with  $\Delta f/\bar{f} \approx 0.3$ . The poloidal wave-number of the QCF is calculated by the 3D ray-tracing code GENRAY, which is found to be  $k_\theta \approx 4\text{--}6 \text{ cm}^{-1}$  or  $k_\theta \rho_s \sim 0.2\text{--}0.4$ , where  $\rho_s = c_s/\omega_{ci}$  is the hybrid ion gyro-radius,  $c_s$  is the sound speed and  $\omega_{ci}$  is the ion gyro-frequency. Therefore, the SOL QCF is a long-wavelength ion-scale fluctuation. The SOL QCF was not observed by the magnetic probe array. One reason might be that the magnetic fluctuations in the  $k_\theta$ -range of the SOL QCF ( $k_\theta \approx 4\text{--}6 \text{ cm}^{-1}$ ) is too weak to be detected by the magnetic probe array on the vessel wall due to the quick decay of the high mode number fluctuations.

The SOL QCF occurs rapidly after each ELM crash and substantially increases the density fluctuation level. The evolution of the SOL density fluctuation between a few ELMs in shot 160511 are demonstrated in Fig. 3. In this case, the SOL mode starts to grow within 10 ms after each large type I ELM and the following small ELMs (Fig. 3(a)). The RMS level of the density fluctuations corresponding to the SOL QCF start to saturate in about 10–20 ms (Fig. 3(b)). Also, an elevated  $D_\alpha$  line intensity are observed during the burst of the SOL QCF (Fig. 3(c)), implying a potential role of the SOL QCF in the enhanced divertor transport and recycling process.

The phase velocity profile of the QCF can be estimated via  $V_{ph} = 2\pi\bar{f}/k_\theta$ , where  $\bar{f} = \sum_f f S(f)/\sum_f S(f)$  with  $S(f)$  the power spectrum density. The calculated phase velocity is a superposition of the  $E_r \times B$  velocity and any other poloidal velocity in the plasma frame. The

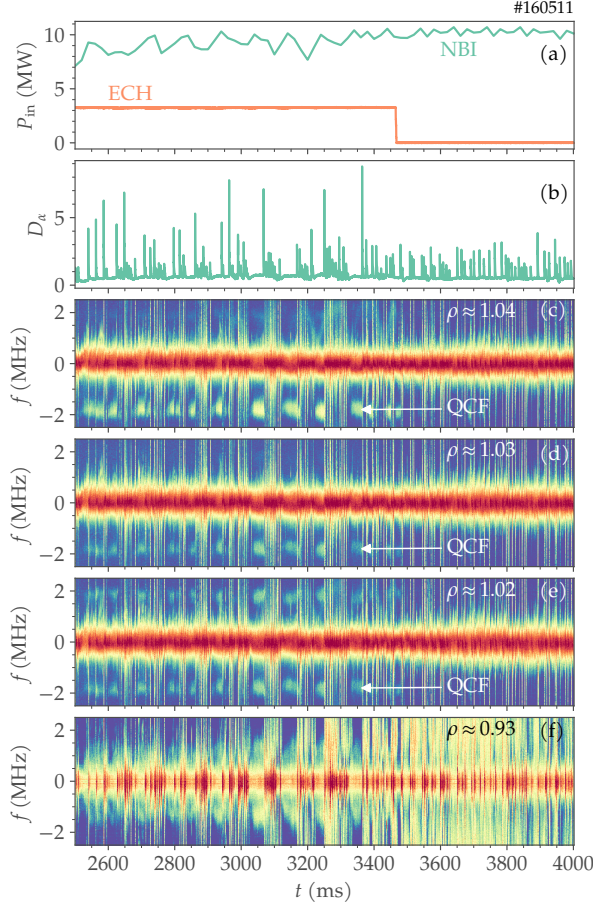


Figure 2. Time traces of (a) input power by NBI (green) and ECH (orange), and (b)  $D_\alpha$  line emission intensity. Contour plots are spectrograms of the density fluctuations measured by the DBS system at both SOL (c)–(e) and pedestal (f) region.

phase velocity of the SOL QCF is found to be in the range of  $-12$  to  $-22$  km/s (teal triangles in Fig. 4). The positive velocity indicates the propagation in the ion diamagnetic drift direction in the lab frame. The mean profiles of  $E_r \times B$  velocities are also obtained at two different time periods, i.e., with (red squares in Fig. 4) and without (blue circles in Fig. 4) detectable SOL QCF. Here, the radial electric field,  $E_r$ , is obtained from the radial force balance equation using the carbon impurity profiles measured by the CER system. The mean  $E_r \times B$  velocities do *not* show significant differences between those two cases. By comparing against the  $E_r \times B$  velocities, we can see the SOL QCF is propagating in the ion diamagnetic drift direction in the plasma frame.

The radial wave-numbers of the SOL QCF can also be estimated using the two-point technique [26]. Figure 5 shows the radial wavenumber-frequency spectrum,  $S(k_r, f)$ , obtained from two

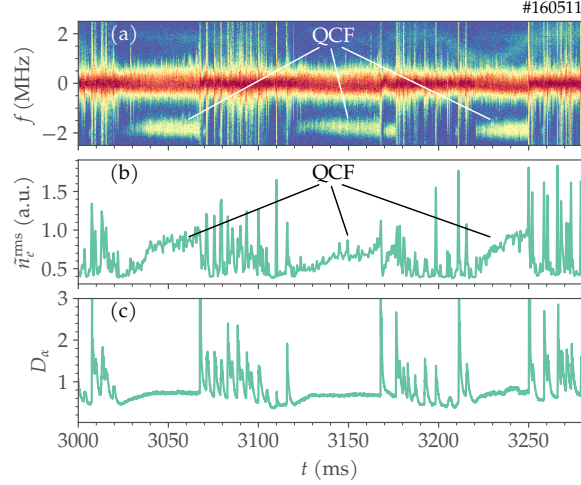


Figure 3. Spectrogram of SOL density fluctuation signals in between ELMs (a), the RMS level of the SOL density fluctuation at  $-1 < f < -2.5$  MHz (b), as  $D_\alpha$  line intensity near outboard divertor strike point (c).

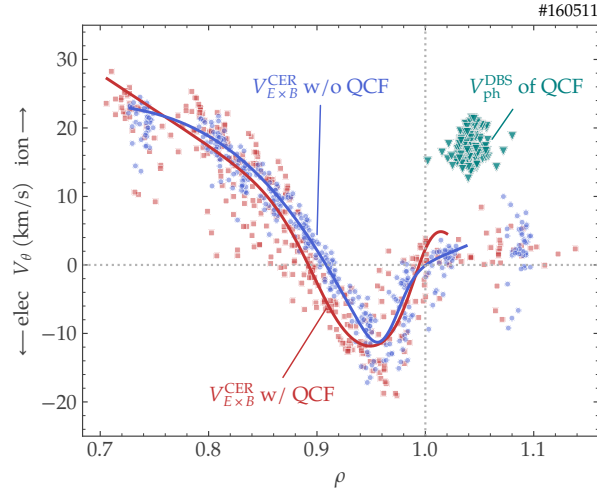


Figure 4. The radial profiles of poloidal phase velocities of SOL QCF measured by DBS (teal triangles), and  $E_r \times B$  velocities given by CER measurements with (red squares) and without (blue circles) SOL QCF, respectively. Solid curves are the spline fits of the scatter points. Positive velocity is in the ion diamagnetic drift direction.

radially separated density fluctuations in the SOL region. One can see a noticeable spot in  $S(k_r, f)$  between 1.5 MHz and 2 MHz which corresponds to the SOL QCF. A positive value of the wave-number indicates a radially outward phase velocity. The spectral-averaged radial wavenumber of the SOL QCF is  $\bar{k}_r = \sum_{k_r} k_r S(k_r, f = f_{\text{QCF}}) / \sum_{k_r} S(k_r, f = f_{\text{QCF}}) \approx 0.5 \text{ cm}^{-1}$ , where the  $S(k_r, f =$

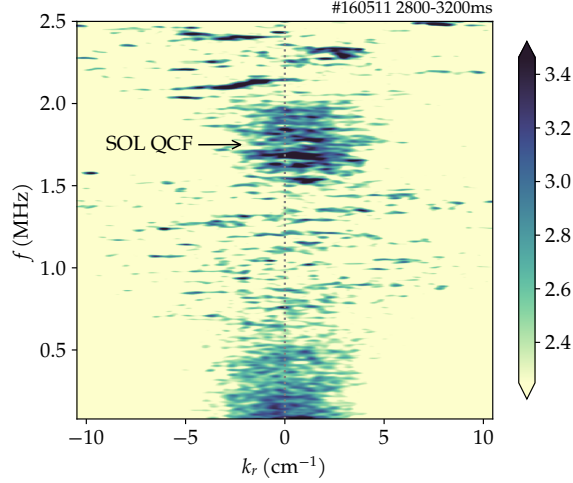


Figure 5. Wavenumber-frequency spectrum,  $S(k_r, f)$ , in the SOL region. The spectrum is calculated using the density fluctuations measured by the channel 1 and 2 of the DBS system. Positive  $k_r$  corresponds to the radially outward direction.

$f_{\text{QCF}}$  is the wavenumber-frequency spectrum in QCF's frequency range. In addition, the spread of the spectral-averaged radial wavenumber is approximately  $\Delta\bar{k}_r \approx 3-4 \text{ cm}^{-1}$ , where  $(\Delta\bar{k})^2 = \sum_{k_r} (k_r - \bar{k}_r)^2 S(k_r, f = f_{\text{QCF}}) / \sum_{k_r} S(k_r, f = f_{\text{QCF}})$ . The radial correlation length of the SOL QCF can be inferred from the spread of the radial wavenumber, i.e.,  $l_{c,r} = 2\pi / (\Delta\bar{k}_r) \approx 1.5-2 \text{ cm}$ , which well exceeds the typical  $\lambda_q$  mapped onto midplane in the DIII-D (about 2-3 mm).

The small radial wavenumber of the SOL QCF may raise a concern about the link between the SOL and the pedestal fluctuations, i.e., whether the SOL QCF is part of a long-range correlation structure extending into the pedestal region. To answer this question, we compute cross-correlation and coherence between the envelopes (fluctuation levels) of the density fluctuations measured at the SOL and the pedestal region (as shown in Fig. 2(c) and (f)). The envelopes are calculated by applying the Hilbert transform to the high-frequency density fluctuations. The coherence between the envelopes of the SOL ( $\tilde{n}_e^{\text{SOL}}$ ) and the pedestal ( $\tilde{n}_e^{\text{ped}}$ ) density fluctuation is weak (blue curve in Fig. 6(a)), except a peak in the frequency range of  $n = 1$  tearing modes ( $f_{\text{TM}} \approx 13 \text{ kHz}$ ). In contrast, the envelopes of two radially separated SOL density fluctuations show larger coherence overall (red curve in Fig. 6(a)). Besides, the time-dependent cross-correlation analysis shows that the phase delay between the envelopes of two SOL fluctuations is close to zero (Fig. 6(b)), while there is no clear phase delay between the envelopes of  $\tilde{n}_e^{\text{SOL}}$  and  $\tilde{n}_e^{\text{ped}}$  (Fig. 6(c)).



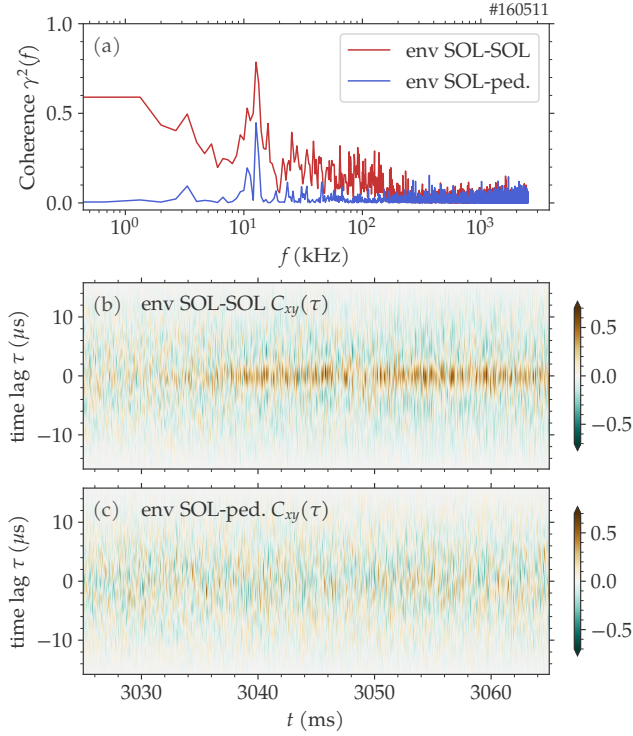


Figure 6. Coherence and cross-correlation analysis. (a) Red curve: coherence between the envelopes of two density fluctuations in SOL (channel-1 vs channel-2 of DBS); blue curve: coherence between the envelopes of  $\tilde{n}_e^{\text{SOL}}$  and  $\tilde{n}_e^{\text{ped}}$ . (b) cross-correlation function between the envelopes of two density fluctuations in SOL. (c) cross-correlation function between the envelopes of  $\tilde{n}_e^{\text{SOL}}$  and  $\tilde{n}_e^{\text{ped}}$  ( $\rho \approx 1.03$  and  $0.94$ ).

The weak cross correlation and coherence indicates that the pedestal fluctuations are not linearly correlated to those of the SOL QCF. Thus, the SOL QCF is unlikely a radial extension of the pedestal fluctuations.

The statistical properties of the SOL QCF are also calculated using DBS density fluctuation signals, but there is no clear features of intermittency. In a typical discharge, the probability density function (PDF) of the SOL QCF is heavier tailed (gray bars in Fig. 7(a)), i.e., shows fatter tails than the Gaussian distribution (blue dashed line in Fig. 7(a)). Here, the corresponding kurtosis of PDF is  $K = 3.1$ , and the Fisher's kurtosis definition is used so that the standard normal distribution has a kurtosis of zero. Also, the PDF is approximately symmetrical and thus leads to a negligible skewness  $S = -0.13$ . The skewness of the SOL QCF is much smaller than that of the blobs in the DIII-D which typically approaches a value of one in the far SOL [6]. The time traces of the kurtosis and skewness are shown in Fig. 7(b) and (c). During the burst of the SOL QCF, the kurtosis of the SOL density fluctuations drops to  $1 < K < 5$  and the skewness drops to a value

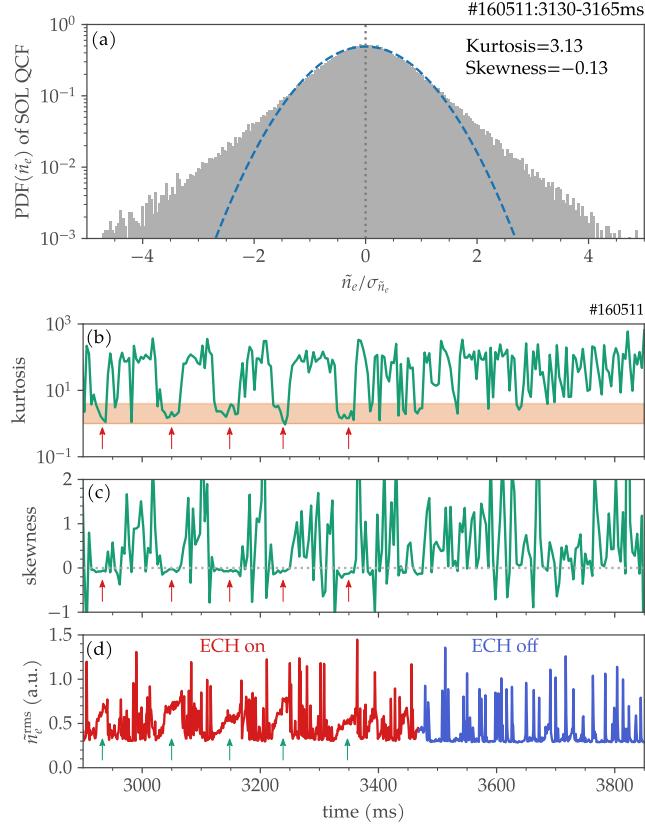


Figure 7. (a) The probability distribution density of the quasi-coherent density fluctuation in the SOL region (gray bars) and the Gaussian fit (blue dashed line) for the distribution. Time traces of the kurtosis (b), skewness (c) and rms level (d) of the density fluctuations in the SOL. The arrows in (b)–(d) indicate the periods with the SOL QCF.

about zero. When there is no SOL QCF observed, the kurtosis of the SOL density fluctuations is typically at higher values, i.e.,  $10 < K < 100$ , and the skewness approaches a value of one. This high kurtosis and skewness in the far SOL region is mainly due to the frequent ELM events. The relatively lower values of kurtosis and skewness of the SOL QCF imply its non-intermittent features.

## B. Enhanced boundary transport by SOL QCF

We also explored the potential effects of the SOL QCF on particle and heat transport into the divertors. The fixed Langmuir probes [22] are employed to provide the plasma parameters on the divertor targets, such as electron density and temperature as well as the particle and

heat fluxes. These divertor quantities are then used to compare against the midplane density fluctuation corresponding to the SOL QCF. Here, we use the ion saturation current density,  $j_{\text{sat}} \propto n_e c_s$  with  $c_s$  the ion sound speed, to indicate the particle flux into the sheath of the divertor targets. In this study, the responses to the large type-I ELMs in all signals are removed. For a typical discharge shown in Fig. 8, the SOL QCF is correlated with elevated divertor electron density and temperature as well as the parallel particle and heat fluxes. During the burst of the SOL QCF, there is a clear increase in the electron density and temperature measured near the strike points in the ‘primary’ divertor (red in Fig. 8(b) and (c)). Also, the ion saturation current density and the parallel heat flux increases during the burst of the SOL QCF (red in Fig. 8(d) and (e)). When the SOL QCF is suppressed, the divertor density, temperature, and corresponding particle and heat fluxes are also reduced (blue in Fig. 8(b)–(e)).

The ion saturation current density and the parallel heat flux are plotted against the midplane density fluctuation level, to see how the divertor fluxes respond to the SOL QCF at the midplane. As shown in Fig. 9, the magnitude of the ion saturation current density,  $j_{\text{sat}}$ , and the parallel heat flux,  $Q_{\parallel}^e$ , is greater during the burst of SOL QCF (e.g.,  $\tilde{n}_e^{\text{rms}} > 0.6$ ). In other words, the SOL QCF can potentially increase the particle and heat fluxes onto the divertor targets by a factor of 2–3. These findings imply the important role of the SOL QCF in the boundary transport processes.

In these discharges, the coverage of the divertor Langmuir probes was not optimized for this plasma shape, so detailed measurements of particle and heat distributions on the divertor targets were not available. Further studies are needed to investigate the effects of the SOL QCF on the profiles of density and temperature, as well as particle and heat fluxes, on the divertor targets.

### C. Influence of boundary profiles

The boundary plasma profiles and their links to the SOL QCF are examined. We collected boundary profiles of electron density, temperature and pressure from 20 shots of the same run-day. The boundary profiles are conditionally averaged for time slices with and without SOL QCF for each shot. The profiles from each shot are then plotted as gray curves in Fig. 10(a)–(f), where the cases with QCF are plotted on the left-hand side and those without SOL QCF are on the right-hand side. Averaging over all 20 shots gives the mean profiles of the electron density, temperature, and pressure (red and blue in Fig 10(a)–(f)). The red and blue curves in

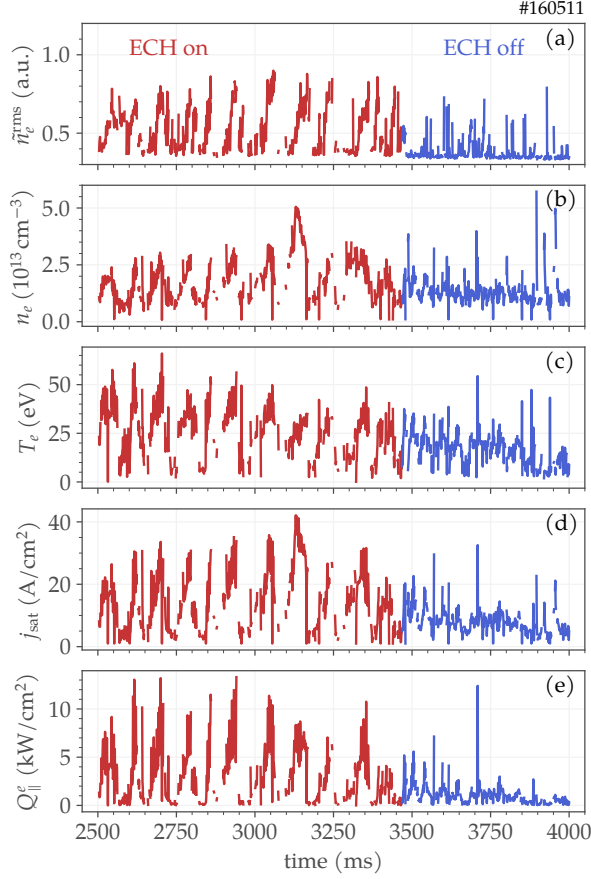


Figure 8. Time traces of the amplitude of the SOL QCF measured by DBS (a), divertor electron density (b), divertor electron temperature (c), the ion saturation current density (d), and the parallel heat flux (e) onto the target in the ‘primary’ (upper) divertor, respectively. Here, the divertor parameters are measured by fixed divertor probes. Red and blue curves correspond to the time with and without the ECH.

each plot represent the mean profiles with and without SOL QCF, respectively. In addition, the corresponding radial gradients with and without SOL QCF are calculated (Fig 10(g)–(l)). Similarly, the conditionally averaged radial gradients for each shot are plotted in gray curves, and the shot-wise average of gradients are plotted in red and blue for the cases with and without SOL QCF, respectively. As shown in Fig. 10(a), during the burst of the QCF SOL, the electron density profile exhibits a shelf-like structure that spans the separatrix and extends into the SOL region. This particular density profile leads to an enhanced SOL density gradient (Fig. 10(g)), which is suspected to drive the SOL QCF.

The SOL density gradient seems to be the most relevant boundary parameters for the SOL

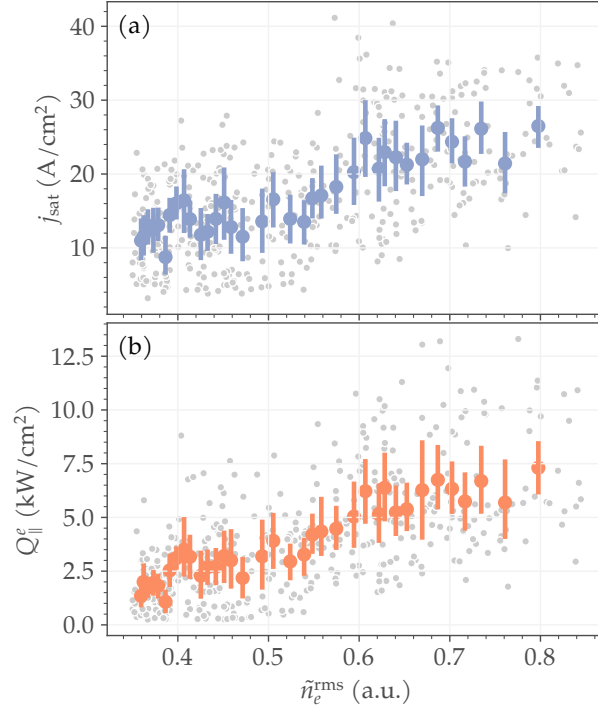


Figure 9. The ion saturation current density (a) and the parallel heat flux (b) plotted against the density fluctuation level corresponding to the SOL QCF. Errorbars show the mean and standard deviation at each density fluctuation level. The underlying gray dots represent the raw data. Both fluxes show clear increasing tendency during the burst of the SOL QCF.

QCF. To investigate the response of the SOL QCF to the SOL density profile, the amplitude of the SOL QCF is compared against the SOL density gradient. Here, the reflectometry diagnostics [27] are employed to provide the measurements of the density profile with higher time resolution ( $\delta t = 1$  ms), so that we can trace the response in each inter-ELM cycle. As shown in Fig. 11, the higher density fluctuation levels of the SOL QCF are associated with higher SOL density gradients. It exhibits a critical density gradient behavior—the density fluctuation shows no clear response at lower density gradient, but increases very rapidly once the critical gradient is exceeded. These findings imply that  $-\nabla n_e^{\text{SOL}}$  plays an important role in the formation of the SOL QCF.

The more general responses of the SOL QCF to the SOL electron density, temperature, and pressure gradients are shown in Fig. 12(a) and (b). The red and blue data points represent the cases with and without SOL QCF observed, respectively. Here, the SOL electron temperature gradient

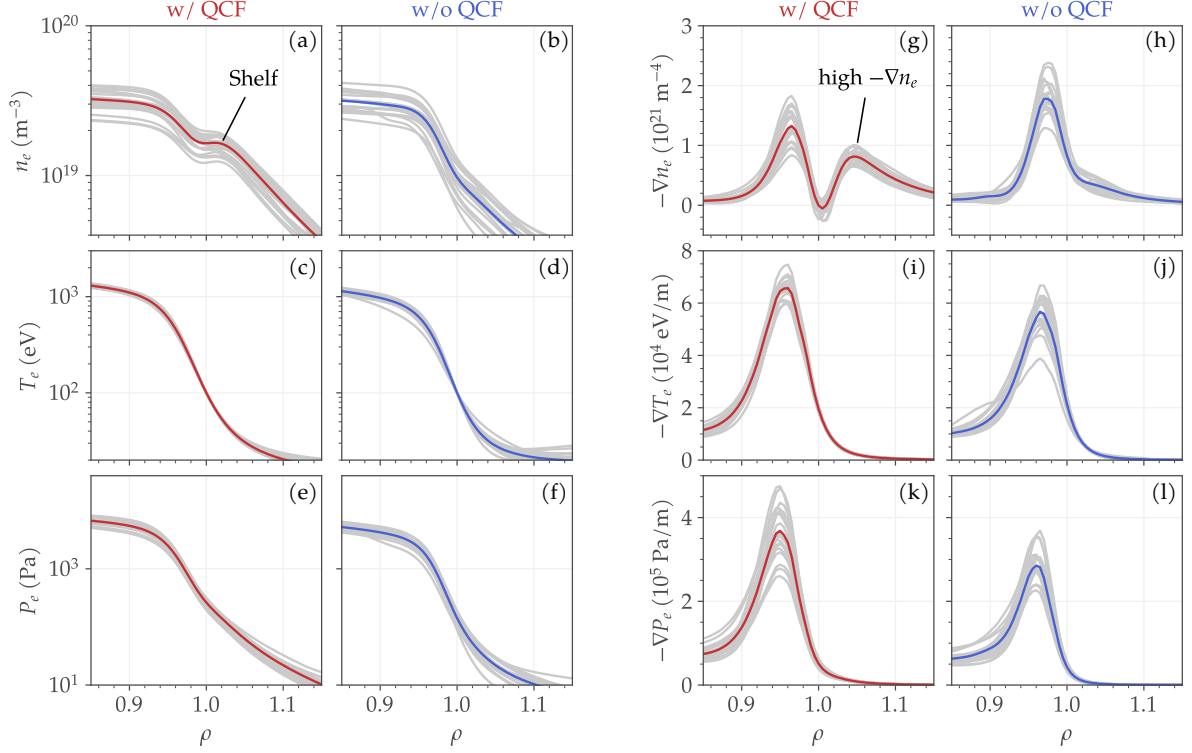


Figure 10. Left panel (a)–(f): boundary profiles of the electron density, temperature, and pressure. Right panel (g)–(l): radial gradients of the electron density, temperature, and pressure. Log-scales are applied in (a)–(f). Red and blue curves correspond to mean profiles with and without SOL QCF, respectively. A shelf-like profile can be identified near the separatrix and is associated with higher SOL density gradient.

$(-\nabla T_e^{\text{SOL}})$  and pressure gradient  $(-\nabla P_e^{\text{SOL}})$  are plotted against SOL density gradients  $(-\nabla n_e^{\text{SOL}})$ . The gradients are averaged over  $1.01 < \rho < 1.08$ . Clearly, the SOL QCF is found to be correlated with higher SOL density gradient (Fig. 12(a)). It may also be associated with higher SOL electron temperature gradient (Fig. 12(a)). However, the relative variation of the SOL electron temperature gradient is much smaller than that of the SOL density gradients. Specifically, the maximum to minimum ratio of  $-\nabla T_e^{\text{SOL}}$  is about 2, while the ratio of  $-\nabla n_e^{\text{SOL}}$  is about 5. As a result,  $-\nabla P_e^{\text{SOL}}$  is almost linearly proportional to  $-\nabla n_e^{\text{SOL}}$ , and the excitation of the SOL QCF is also associated with higher  $-\nabla P_e^{\text{SOL}}$  values (Fig. 12(b)). These findings suggest that either  $-\nabla n_e^{\text{SOL}}$  or  $-\nabla P_e^{\text{SOL}}$  can serve as the free energy drive for the SOL QCF.

The SOL and divertor collisionality has been previously observed to have an influence on the dynamics of the SOL turbulence such as the blobs [16], and thus may also affect the response of the SOL QCF. The effective SOL collisionality,  $\Lambda_{\text{eff}}^{\text{SOL}} = \nu_{ei} L_{\parallel} \Omega_i / (\Omega_e c_s)$ , is used to characterize

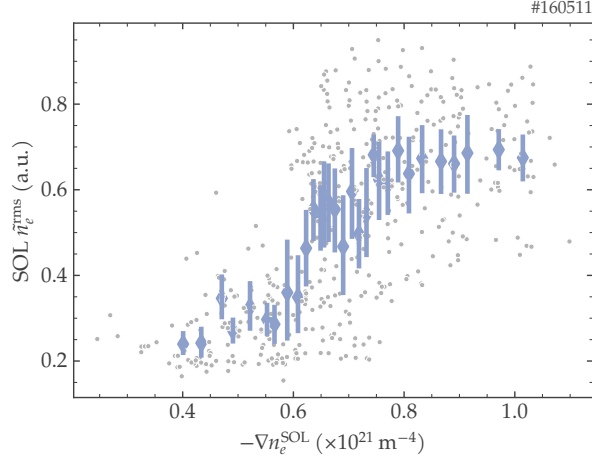


Figure 11. The response of the SOL density fluctuation levels in the QCF frequency range (1.5–2.5 MHz in DBS signals) to the SOL density gradient (by reflectometry). The purple errorbars show the mean and standard deviation of the density fluctuation level at each SOL density gradient. The underlying gray dots indicate the raw data.

the electron-ion collisional dynamics in the SOL region [16, 28]. Here,  $\nu_{ei}$  is the electron-ion collision rate,  $L_{\parallel}$  is the connection length,  $c_s$  is the sound speed, and  $\Omega_{e,i}$  is the electron/ion gyro-frequency. However, there is no obvious threshold in the  $\Lambda_{\text{eff}}^{\text{SOL}}$  that distinguishes the stable and unstable cases for the SOL QCF, indicating that the SOL QCF is *not* sensitive to the collisional effects (Fig. 12(c)).

#### D. Linear simulation using BOUT++

A linear simulation using the BOUT++ framework with a reduced 5-field fluid model has been carried out and compared to the observations shown in previous sections. This model evolves five perturbed variables, i.e., ion density, ion and electron temperature, magnetic flux, and the vorticity [29, 30]. This reduced 5-field model includes the ideal and resistive peeling-ballooning physics, as well as diamagnetic and  $E \times B$  drift. The simulated domain in normalized poloidal flux is  $0.95 < \psi_n < 1.10$ , and the grid resolution is  $N_{\psi_n} = 256$  in the radial direction and  $N_y = 64$  in the poloidal direction. The resistivity  $\eta$  is considered as Spitzer-Härm resistivity. Since it is based on the Braginskii reduced fluid equations, the model is only suitable for the simulation of long wavelength turbulence with  $k_{\perp} \rho_s < 1$ . This wavenumber range covers the scales of the SOL

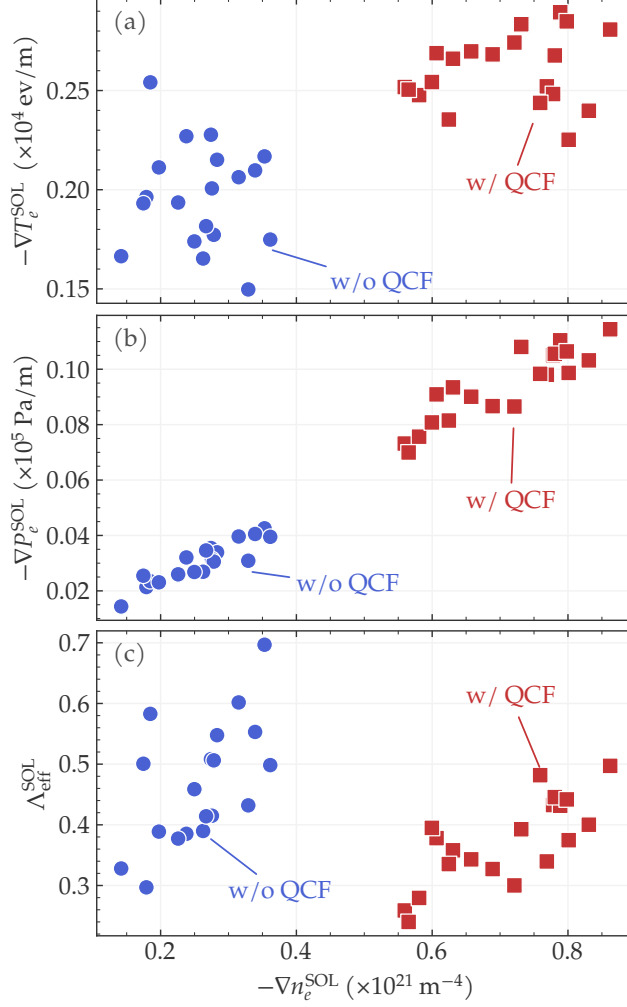


Figure 12. The SOL temperature gradient (a), pressure gradient (b), and the effective collisionality (c) plotted against the SOL density gradient. The parameters are averaged over  $1.01 < \rho < 1.08$ . Red squares and blue circles correspond to cases with and without SOL QCFs, respectively.

QCF ( $k_{\perp}\rho_s = 0.2 - 0.4$ ). BOUT++ employs only the toroidal mode number,  $n$ , as the independent variable for the linear scan, and the poloidal mode number,  $m$ , is determined via a local effective safety factor  $q_{\text{eff}}$  inferred from the local pitch angle [31], i.e.,  $m = nq_{\text{eff}}$ . Thus, the effective poloidal wavenumber can be defined as  $k_{\theta}^{\text{eff}} = nq/a$ , where  $a$  is the plasma minor radius,  $m$  and  $n$  are the poloidal and toroidal mode number respectively. More details about the BOUT++ 5-field model deployed in this study can be found in previous publications [29, 30].

The linear BOUT++ simulations show that the density perturbation can be destabilized in the SOL region. When the SOL QCF is observed, the density gradient increases significantly in the SOL region (red in Fig. 13(a)). According to the BOUT++ linear simulations at  $k_{\perp}\rho_s \approx 0.3$ , the



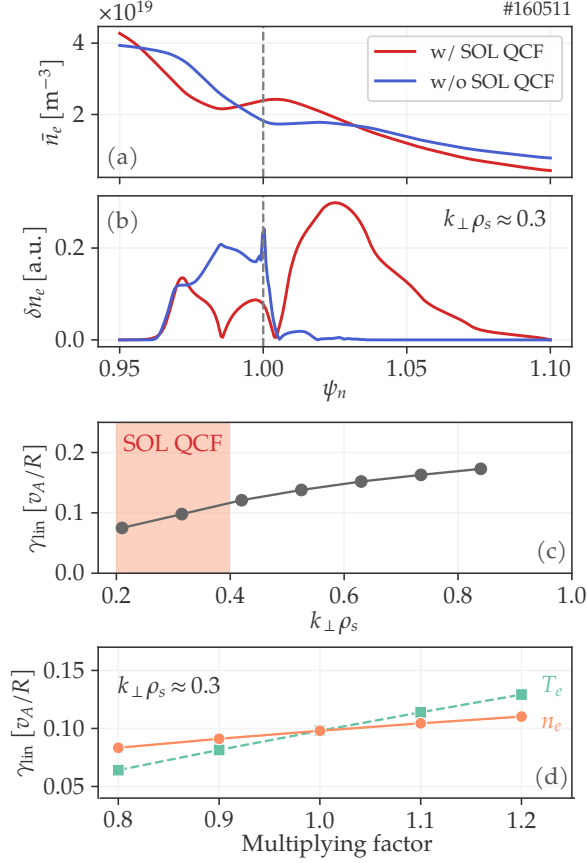


Figure 13. (a) Input density profiles with (red) and without (blue) SOL QCF observed. (b) Density perturbation profiles with (red) and without (blue) SOL QCF observed with  $k_{\perp} \rho_s \approx 0.3$ . (c) Linear growth rates calculated with experimental profile (red in (a)) at different wavenumber; the shaded area indicates the wavenumber range of the SOL QCF. (d) Linear growth rates calculated with different scale factors of the electron density (orange) and temperature (green) profiles.

density perturbation,  $\delta n = \tilde{n}/\bar{n}$ , peaks in the SOL region (red in Fig. 13(b)). The peak of this density perturbation is located at  $\psi_n \approx 1.02$ – $1.03$ , corresponding to the location with maximum density gradient in the SOL region. The radial width (FWHM) of this density perturbation is about 1.3 cm. When the SOL QCF is not observed, the density profile is more flattened in the SOL (blue in Fig. 13(a)), and the SOL density perturbation is stabilized (blue in Fig. 13(b)). Also, the pedestal density perturbation ( $0.95 < \psi_n < 1$ ) becomes the dominant mode when the SOL QCF does not appear (blue in Fig. 13(b)). The simulated mode is most unstable at the outer midplane, bad curvature region, and propagates in the ion diamagnetic drift direction, indicating its interchange-like nature. Above all, the propagation direction, the peak location, and the radial

width of the SOL density perturbation are in agreement with the experimental observations by the DBS system.

The linear growth rate of the SOL density perturbation are calculated at different turbulence scales ( $0.2 < k_{\perp}\rho_s < 0.9$ ), using the experimental profiles with SOL QCF observed. The SOL density perturbation is found to be unstable for a wide range of the poloidal wavenumbers which covers the range of the SOL QCF (Fig. 13(c)).

To identify the dominant free energy drive for the SOL density perturbation, the density and temperature profiles are multiplied by a factor, ranging from 0.8 to 1.2, with  $k_{\perp}\rho_s \approx 0.3$  in the simulation. It is a common scanning technique used in BOUT++ simulations [29]. The local quantity and gradient are thus changed accordingly, while the scale lengths are fixed. As shown in Fig. 13(c), the linear growth rate increases as the density (orange) or the temperature (green) profiles are raised. Since the increased density and temperature profiles can enhance the linear growth rate of the SOL density perturbation, its free energy source is likely attributed to the SOL pressure gradient.

#### IV. DISCUSSION

In this study, we have identified the quasi-coherent fluctuation as an important turbulence structure that may influence the SOL turbulent transport in the high-power, high-performance hybrid plasmas. The SOL QCF is correlated with the steepened SOL density and pressure gradients, due to a shelf-like density profile across the separatrix. Also, this QCF is an ion-scale long-wavelength fluctuation, and propagates in the ion diamagnetic drift direction in the plasma frame. The linear simulation using BOUT++ shows that the SOL density perturbation is most unstable at the outer midplane bad curvature region, and the SOL pressure gradient can provide the free energy drive for this mode. These findings indicate that the SOL QCF is an interchange-like mode.

Conventionally, the blobs have been considered the dominant turbulence structure in the SOL region [14]. Some differences between the SOL QCF and blobs, as well as the implications to the SOL transport studies, can be drawn:

- The SOL QCF is a long-lived mode during the inter-ELMs period, while the blobs are intermittent events. This is also reflected in the probability density function (PDF): the PDF of the SOL QCF is symmetrical and has a small skewness value, while the blobs' PDF

is featured by a substantial skewness in the SOL region [6]. Thus, the SOL QCF may result in more contribution to SOL transport than the blobs over a long period of time, which might be an issue for long-pulse and steady-state operations.

- The SOL QCF shows little dependence on the effective SOL collisionality,  $\Lambda_{\text{eff}}^{\text{SOL}}$ , while the blobs' size and the induced transport is found to increase significantly as  $\Lambda_{\text{eff}}^{\text{SOL}}$  is raised [16, 32]. It is therefore expected that in low-collisionality plasmas the blobs and its induced transport would be reduced, while the SOL QCF would be less affected. The collisionality of plasma in future devices will probably be much lower than that in present devices. Hence, the control of the SOL QCF should be taken in to account in future fusion devices.
- The SOL QCF is a radially localized mode with a radial correlation length of  $l_{c,r} \approx 1.5\text{--}2$  cm, while the blobs are coherent objects that often propagate radially for a long distance. So, the SOL QCF may be less likely to hit the mainchamber wall and thus have less impact than the blobs on the recycling and plasma-material interaction in the mainchamber.

Due to the observations and implications discussed above, the SOL QCF might become an issue for the control of the plasma-material interaction (PMI) in future fusion devices operated with high-power high- $\beta_N$  scenarios. The observation of the SOL QCF may also raise a challenge for developing more accurate transport and PMI modeling in the boundary region of high- $\beta_N$  plasmas. Clearly, further research is needed to provide more detailed measurements of the SOL QCF and its influence on SOL transport, including its effects on the particle and heat deposition on the divertor targets and the mainchamber wall.

## V. SUMMARY

To summarize, a quasi-coherent density fluctuation (QCF) has been observed in the SOL region of high-power, high-performance plasmas with ECH injection and near double-null divertor configuration on the DIII-D tokamak. The SOL QCF appears rapidly after the preceding ELM within 10 ms. This mode is correlated with substantially enhanced particle and heat fluxes (e.g., by a factor of 2–3) onto the divertor targets, indicating its potential effects on the SOL transport in high- $\beta_N$  plasmas. The SOL QCF is associated with higher SOL electron density and pressure gradients due to a shelf-like density profile across the separatrix. The QCF propagates in the

ion diamagnetic drift direction  $V_{\text{ph}} \approx 15\text{--}20$  km/s in the plasma frame and poloidal wavenumber  $k_{\theta}\rho_s \approx 0.2\text{--}0.4$ . The SOL QCF propagates outward in the radial direction with small radial wavenumber  $k_r\rho_s \approx 0.03$ , and the correlation length is about 1.5–2 cm. This SOL QCF does not show clear dependence on the effective SOL collisionality  $\Lambda_{\text{eff}}^{\text{SOL}}$ . These properties differ from those of the blobs that are conventionally considered as the dominant SOL turbulence structures.

A linear simulation has been performed using BOUT++ with a 5-field reduced model across the separatrix ( $0.95 < \psi_n < 1.10$ ). The simulation results confirm that a density perturbation can be driven by the elevated SOL pressure gradient at the outer midplane bad curvature region. The mode's propagation direction, peak location, and radial width are in agreement with the experimental observations.

In conclusion, the SOL QCF is likely an interchange-like instability driven by the SOL pressure gradients. It extends from the separatrix to the far SOL region, and leads to significantly enhanced particle and heat fluxes onto the divertor targets. The presence of the SOL QCF may challenge present boundary modeling of high- $\beta_N$  hybrid plasmas, and calls for more detailed work to evaluate its impact on the SOL transport and plasma-material interactions.

## ACKNOWLEDGMENTS

The authors thank Dr. B. Grierson and Dr. R. Buttery for their insightful comments on this paper. This material is based upon work supported by the U.S. Department of Energy, Office of Science, Office of Fusion Energy Sciences, using the DIII-D National Fusion Facility, a DOE Office of Science user facility, under Awards DE-FC02-04ER54698, DE-SC0019352, DE-FG02-08ER54984, and DE-NA0003525.

**Disclaimer:** This report was prepared as an account of work sponsored by an agency of the United States Government. Neither the United States Government nor any agency thereof, nor any of their employees, makes any warranty, express or implied, or assumes any legal liability or responsibility for the accuracy, completeness, or usefulness of any information, apparatus, product, or process disclosed, or represents that its use would not infringe privately owned rights. Reference herein to any specific commercial product, process, or service by trade name, trademark, manufacturer, or otherwise does not necessarily constitute or imply its endorsement, recommendation, or favoring by the United States Government or any agency thereof. The views and opinions of authors expressed herein do not necessarily state or reflect those of the United

States Government or any agency thereof.

---

- [1] J. W. Hughes, D. A. Mossessian, A. E. Hubbard, B. LaBombard, and E. S. Marmor, [Physics of Plasmas](#) **9**, 3019 (2002).
- [2] T. H. Osborne, R. J. Groebner, L. L. Lao, A. W. Leonard, R. Maingi, R. L. Miller, G. D. Porter, D. M. Thomas, and R. E. Waltz, [Plasma Physics and Controlled Fusion](#) **40**, 845 (1998).
- [3] C. S. Pitcher, A. H. Boozer, H. Murmann, J. Schweinzer, W. Suttrop, and H. Salzmann, [Physics of Plasmas](#) **4**, 2577 (1997).
- [4] W. Suttrop, M. Kaufmann, H. J. d. Blank, B. Brüsehaber, K. Lackner, V. Mertens, H. Murmann, J. Neuhauser, F. Ryter, H. Salzmann, J. Schweinzer, J. Stober, H. Zohm, and t. A. U. Team, [Plasma Physics and Controlled Fusion](#) **39**, 2051 (1997).
- [5] A. Loarte, B. Lipschultz, A. S. Kukushkin, G. F. Matthews, P. C. Stangeby, N. Asakura, G. F. Counsell, G. Federici, A. Kallenbach, K. Krieger, A. Mahdavi, V. Philipps, D. Reiter, J. Roth, J. Strachan, D. Whyte, R. Doerner, T. Eich, W. Fundamenski, A. Herrmann, M. Fenstermacher, P. Ghendrih, M. Groth, A. Kirschner, S. Konoshima, B. LaBombard, P. Lang, A. W. Leonard, P. Monier-Garbet, R. Neu, H. Pacher, B. Pegourie, R. A. Pitts, S. Takamura, J. Terry, E. Tsitrone, t. I. S.-o. Layer, and D. Group, [Nuclear Fusion](#) **47**, S203 (2007).
- [6] J. A. Boedo, D. L. Rudakov, R. A. Moyer, G. R. McKee, R. J. Colchin, M. J. Schaffer, P. G. Stangeby, W. P. West, S. L. Allen, T. E. Evans, R. J. Fonck, E. M. Hollmann, S. Krasheninnikov, A. W. Leonard, W. Nevins, M. A. Mahdavi, G. D. Porter, G. R. Tynan, D. G. Whyte, and X. Xu, [Physics of Plasmas](#) **10**, 1670 (2003).
- [7] M. Endler, H. Niedermeyer, L. Giannone, E. Kolzhauer, A. Rudyj, G. Theimer, and N. Tsois, [Nuclear Fusion](#) **35**, 1307 (1995).
- [8] B. LaBombard, R. L. Boivin, M. Greenwald, J. Hughes, B. Lipschultz, D. Mossessian, C. S. Pitcher, J. L. Terry, and S. J. Zweben, [Physics of Plasmas](#) **8**, 2107 (2001).
- [9] B. LaBombard, M. V. Umansky, R. L. Boivin, J. A. Goetz, J. Hughes, B. Lipschultz, D. Mossessian, C. S. Pitcher, J. L. Terry, and A. Group, [Nuclear Fusion](#) **40**, 2041 (2000).
- [10] G. Y. Antar, M. Tsalas, E. Wolfrum, and V. Rhode, [Plasma Physics and Controlled Fusion](#) **50**, 095012 (2008).
- [11] S. I. Krasheninnikov, [Physics Letters A](#) **283**, 368 (2001).

- [12] S. J. Zweben, W. M. Davis, S. M. Kaye, J. R. Myra, R. E. Bell, B. P. LeBlanc, R. J. Maqueda, T. Munsat, S. A. Sabbagh, Y. Sechrest, and D. P. S. and, [Nuclear Fusion](#) **55**, 093035 (2015).
- [13] S. J. Zweben, J. R. Myra, W. M. Davis, D. A. D’Ippolito, T. K. Gray, S. M. Kaye, B. P. LeBlanc, R. J. Maqueda, D. A. Russell, and D. P. S. and, [Plasma Physics and Controlled Fusion](#) **58**, 044007 (2016).
- [14] J. A. Boedo, [Journal of Nuclear Materials Proceedings of the 18th International Conference on Plasma-Surface Interactions in Controlled Fusion Device](#), **390-391**, 29 (2009).
- [15] G. Fuchert, G. Birkenmeier, D. Carralero, T. Lunt, P. Manz, H. W. Müller, B. Nold, M. Ramisch, V. Rohde, and U. Stroth, [Plasma Physics and Controlled Fusion](#) **56**, 125001 (2014).
- [16] D. Carralero, P. Manz, L. Aho-Mantila, G. Birkenmeier, M. Brix, M. Groth, H. W. Müller, U. Stroth, N. Vianello, E. Wolfrum, ASDEX Upgrade team, JET Contributors, and EUROfusion MST1 Team, [Physical Review Letters](#) **115**, 215002 (2015).
- [17] T. W. Petrie, T. Osborne, M. E. Fenstermacher, J. Ferron, R. Groebner, B. Grierson, C. Holcomb, C. Lasnier, A. Leonard, T. Luce, M. Makowski, F. Turco, W. Solomon, B. Victor, and J. Watkins, [Nuclear Fusion](#) **57**, 086004 (2017).
- [18] F. Turco, C. C. Petty, T. C. Luce, T. N. Carlstrom, M. A. Van Zeeland, W. Heidbrink, F. Carpanese, W. Solomon, C. T. Holcomb, and J. R. Ferron, [Physics of Plasmas](#) **22**, 056113 (2015).
- [19] W. A. Peebles, T. L. Rhodes, J. C. Hillesheim, L. Zeng, and C. Wannberg, [Rev. Sci. Instrum.](#) **81**, 5 (2010).
- [20] J. R. Ferron, T. A. Casper, E. J. Doyle, A. M. Garofalo, P. Gohil, C. M. Greenfield, A. W. Hyatt, R. J. Jayakumar, C. Kessel, J. Y. Kim, T. C. Luce, M. A. Makowski, J. Menard, M. Murakami, C. C. Petty, P. A. Politzer, T. S. Taylor, and M. R. Wade, [Physics of Plasmas](#) **12**, 056126 (2005).
- [21] D. Eldon, B. D. Bray, T. M. Deterly, C. Liu, M. Watkins, R. J. Groebner, A. W. Leonard, T. H. Osborne, P. B. Snyder, R. L. Boivin, and G. R. Tynan, [Review of Scientific Instruments](#) **83**, 10E343 (2012), publisher: American Institute of Physics.
- [22] J. G. Watkins, D. Taussig, R. L. Boivin, M. A. Mahdavi, and R. E. Nygren, [Review of Scientific Instruments](#) **79**, 10F125 (2008), publisher: American Institute of Physics.
- [23] C. Chrystal, K. H. Burrell, B. A. Grierson, S. R. Haskey, R. J. Groebner, D. H. Kaplan, and A. Briesemeister, [Review of Scientific Instruments](#) **87**, 11E512 (2016), publisher: American Institute of Physics.
- [24] G. R. McKee, R. J. Fonck, M. W. Shafer, I. U. Uzun-Kaymak, and Z. Yan, [Review of Scientific Instruments](#) **81**, 10D741 (2010).
- [25] A. P. Smirnov, R. W. Harvey, and K. Kupfer, [Bull. Amer. Phys. Soc.](#) **39**, 1626 (1994).

- [26] J. M. Beall, Y. C. Kim, and E. J. Powers, [Journal of Applied Physics](#) **53**, 3933 (1982).
- [27] L. Zeng, W. A. Peebles, E. J. Doyle, T. L. Rhodes, N. Crocker, X. Nguyen, C. W. Wannberg, and G. Wang, [Review of Scientific Instruments](#) **85**, 11D843 (2014).
- [28] J. R. Myra, D. A. D'Ippolito, D. P. Stotler, S. J. Zweben, B. P. LeBlanc, J. E. Menard, R. J. Maqueda, and J. Boedo, [Physics of Plasmas](#) **13**, 092509 (2006).
- [29] Z.-Y. Li, X. Q. Xu, N.-M. Li, V. S. Chan, and X.-G. Wang, [Nuclear Fusion](#) **59**, 046014 (2019).
- [30] T. Y. Xia and X. Q. Xu, [Nuclear Fusion](#) **55**, 113030 (2015).
- [31] B. D. Dudson, M. V. Umansky, X. Q. Xu, P. B. Snyder, and H. R. Wilson, [Computer Physics Communications](#) **180**, 1467 (2009).
- [32] D. A. Russell, J. R. Myra, and D. A. D'Ippolito, [Physics of Plasmas](#) **14**, 102307 (2007), publisher: American Institute of Physics.